Reflectometry Study of Thin Metal Foil Perturbation by a Moderate Intensity Laser Pulse

5.1 Introduction

In chapters Ch.3 and Ch.4 I introduced a few basic concepts on the interaction between a laser pulse and a solid target. Here I focus on the propagation of the shock wave through the bulk and in particular on the evolution of the shock effects on the non irradiated surface (the back surface).

The detrimental effects produced by a laser pedestal on the back surface can reduce or destroy the target normal sheath acceleration (TNSA) according to the timescale of propagation of the shock wave through the thin foil. From the moment the interaction begins between the pulse pedestal and the overdense matter, the shock wave starts propagating. Once it arrives at the back side of the foil, a new plasma starts expanding in that direction: when a sufficient plasma gradient exists on the surface, the TNSA acceleration is reduced due to the lengthening of the Debye length.

In this experiment I use a short laser pulse to monitor the evolution of the electron temperature on the back side of a thin metal foil. The electron temperature is measured through the change in reflectivity of the metal surface. The shock wave is created by a femtosecond laser ($\tau = 150fs$, $I \approx 10^{15}W/cm^2$) with the same characteristics than the one used for the experiment in Ch.4. This, in turns, will enable us to close the loop between the gradient scale length that is created on the front surface (Fig.4.16) and the

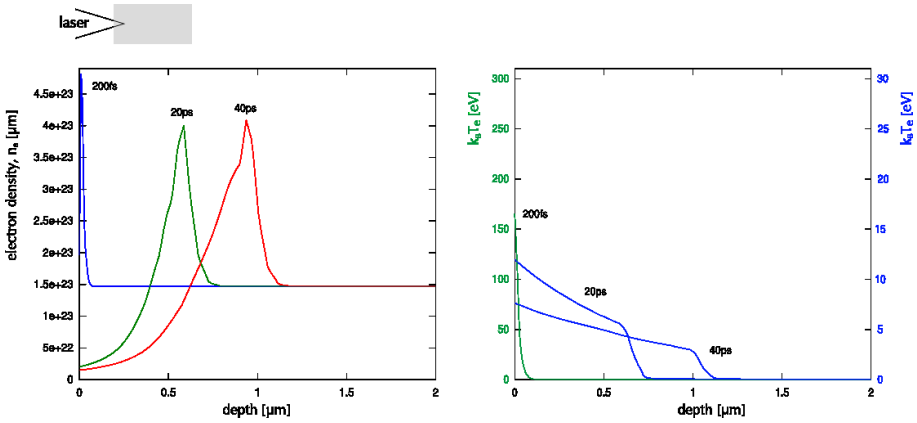

Figure 5.1: Excerpt from the simulations in Fig.4.13 for the evolution beyond the target boundary. *(left)* The shock propagates deeper into the bulk; *(right)* the evolution of the electron temperature. (The 20*ps* and the 40*ps* plots in the right graph are referred to the rightmost scale of temperature).

propagation of the shock through the bulk material.

5.2 Reflectometry Measurements of a Metallic Surface

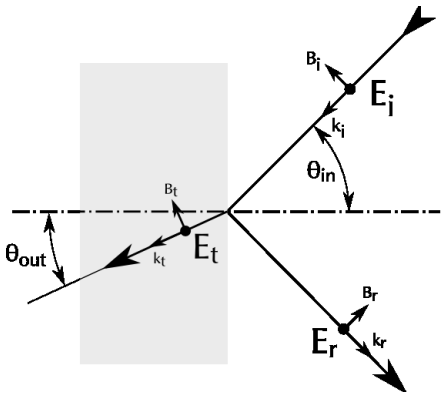

Figure 5.2: Reflection of an S-polarized wave.

The reflectivity of a cold metallic surface, when no density gradient is present, is calculated from the Fresnel coefficients. Let's consider the problem in the geometry depicted in Fig.5.2. When the S-polarized wave arrives at the interface between the metal (ω_{pe},

ε) and the vacuum (ε_0), the reflected and refracted waves are produced. The calculation is carried out by setting the three fields $\underline{\mathrm{E}}_i(\underline{\mathrm{x}}, t)$, $\underline{\mathrm{E}}_r(\underline{\mathrm{x}}, t)$ and $\underline{\mathrm{E}}_t(\underline{\mathrm{x}}, t)$[1] to satisfy the continuity relationship on the interface. Having defined $r_S = E_r/E_i$, it results:

$$r_S = \frac{\cos\theta - \sqrt{\varepsilon - \sin^2\theta}}{\cos\theta + \sqrt{\varepsilon - \sin^2\theta}} \tag{5.1}$$

which defines the reflectivity coefficient as

$$R_S = |r_S|^2, \tag{5.2}$$

where θ is the impinging angle and ε the (complex) dielectric constant for the metal. From the Drude model it holds

$$\varepsilon = 1 - \frac{\omega_{pe}^2}{\omega\,(\omega - \mathrm{i}\nu_{ei})} \tag{5.3}$$

which inserts the contribution of the electron-ion collision frequency ν_{ei}. For an over-dense material $\left(\frac{n_e}{n_c} \gg 1\right)$ the behaviour is defined by the ν_{ei}/ω ratio. If $\nu_{ei}/\omega < 1$, the medium has a good reflectivity when its collisionality is low, i.e. for temperatures lower than some eV or higher than several tens of eV. To estimate the term ν_{ei} I use the Eidmann-Hüller interpolation between the Spitzer collision frequency for the hot plasma and the electron-phonon collision frequency for the cold limit[14, 94, 20].

The Spitzer formula for the collision frequency is

$$\nu_{Spitzer} = \frac{4}{3}\sqrt{2\pi}\,\frac{Z^* e^4}{16\pi^2\varepsilon_0^2}\,\frac{m_e n_e}{(m_e k_B T_e)^{3/2}}\ln\left(\Lambda'\right) \tag{5.4}$$

where $\Lambda' = \left(1 + (b_{max}/b_0)^2\right)^{1/2}$ is the Coulomb parameter. The terms b_0 and b_{max} are respectively *(i)* the impact factor for a $\pi/2$ deflection in a Rutherford scattering and *(ii)* the maximum impact factor for a deflection to happen, before the electrostatic field of the scattering center is shielded by the plasma. Here they are used in the form

[1] Usual representation: $\underline{\mathrm{E}} = \underline{\mathrm{E}}_0 \exp\left[\underline{\mathrm{k}}\underline{\mathrm{x}} - \omega t\right]$.

$$\begin{cases} b_{max} &= \sqrt{\dfrac{k_B T_e}{m_e}} \dfrac{1}{\max(\omega,\, \omega_{pe})} \\ b_0 &= \max\left(\dfrac{h}{\sqrt{k_B T_e m_e}},\, \dfrac{Z^* e^2}{4\pi\varepsilon_0} \dfrac{1}{k_B T_e} \right), \end{cases} \tag{5.5}$$

where to the common corrections (λ_{Debye} for b_{max} and classical calculation for b_0) are added[2].

In the cold limit the considered collision frequency is the $\nu_{el-phonon}$ between electrons in the material and phonons:

$$\nu_{el-phonon} = k_s \frac{e^2}{4\pi\varepsilon_0 \hbar v_F} \left(2 - \frac{v_F^2}{c^2}\right) \left[1 + \left(0.13 \frac{\hbar\omega_{pi}}{k_B T_i}\right)^2\right]^{1/2} \frac{k_B T_i}{\hbar} \tag{5.6}$$

$$\approx 2k_s \frac{e^2 k_B T_i}{4\pi\varepsilon_0 \hbar^2 v_F} \tag{5.7}$$

where ω_{pi} is the ion plasma frequency, T_i the ion temperature and it is used the expression for the Fermi's velocity $v_F = (\hbar/m_e)\left(3\pi^2 n_e\right)^{1/3}$. The k_s parameter in (5.7) is calculated to fit the tabulated data[3].
The set of frequencies between the two extreme cases is extrapolated by

$$\nu_{ei}^{-1} = \nu_{Spitzer}^{-1} + \nu_{el-phonon}^{-1}. \tag{5.8}$$

The evolution of the reflectivity is numerically obtained from (5.2) with the values obtained from (5.8) for different electron temperatures in the case of an impinging angle of $\theta = \pi/4$ and $\omega_{laser} = 2\pi c/\left(\lambda_{probe} = 400nm\right)$.

Notes on Ion temperature The collision frequency in the cold limit depends on the ion temperature. For a given electron temperature, a decrease in the ion temperature will reduce the collisionality in the cold limit, which increases the contribution of ν_{cold} (5.7) to ν_{ei} (5.8); this, in turns, increases the depth of the reflectivity drop (see Fig.5.3).

[2]The max() term in (5.5)-i corrects the λ_D when an evanescent wave is present; the first term in (5.5)-ii sets that no impact parameter smaller than the deBroglie's wavelength of the impinging particle should be considered.

[3]The approximation to the cold metal solid is done via $v_F \ll c$ and $\hbar\omega_{pi} \ll k_B T_i$. It is set $k_s = 58.9$, calculated from the condition $\nu_{el-phon}\left(T = 300K\right) = n_e e^2 \rho / m_e$, being the tabulated resistivity of aluminum $\rho\left(T = 300K\right) = 26.50n\Omega \cdot m$.

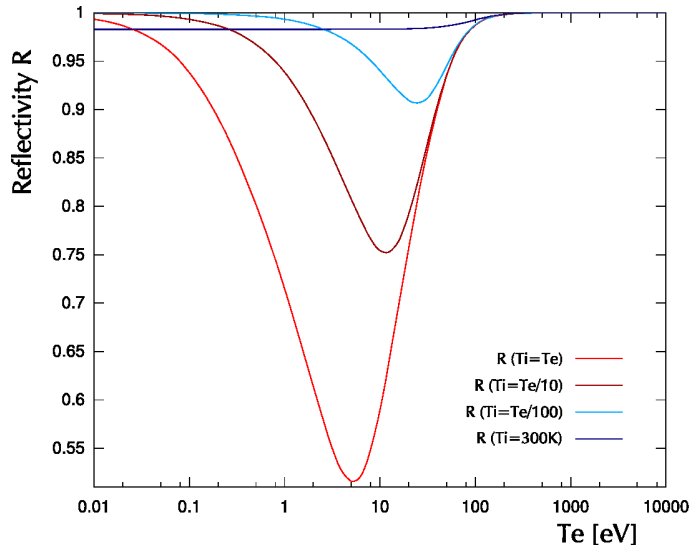

Figure 5.3: Reflectivity vs. electronic temperature from the Eidmann-Huller interpolation of electron-ion collision frequency, for an Aluminum bulk at solid density with $\lambda = 400nm$ s-polarized light impinging at 45°. Different ion temperatures are shown.

5.3 Experimental Setup

As in the previous experiment two beams are obtained from the laser chain of the *Salle Verte* (Ch.4). The most intense one is focused to produce a plasma on thin Aluminum foils ($3\mu m$, $2\mu m$ and $800nm$); the less intense is delayed through a variable delay line, doubled in frequency and reflected and diffused by the rear surface of the metallic target. Here's a brief description of the realized setup.

Pump Beam The beam is focused by a single lens of $f = 1000mm$. The focal spot is sent by a removable mirror to a microscope objective and imaged on a 12bit camera (Fig.5.4-5); the image is used to correct the lens tilt, controlling the aberrations, and to measure the size and the energy content of the focal spot. The obtained spot exhibits (Fig.5.5) an average diameter on the $1/e^2$ (fwhm) of approximately $58\mu m$ ($34\mu m$). The corresponding Rayleigh range is $z_0 = 3.5mm$. The total energy on the *pump* beam line is about $E_L = 20mJ$, which results in a peak intensity of $I_0 = 8 \times 10^{15} W/cm^2$.

Probe Beam The *probe* beam, with energy lower than $2mJ$ is first reduced in diameter by a telescope, $f_1 = 500mm$, $f_2 = 100mm$. This operation has the dual purpose

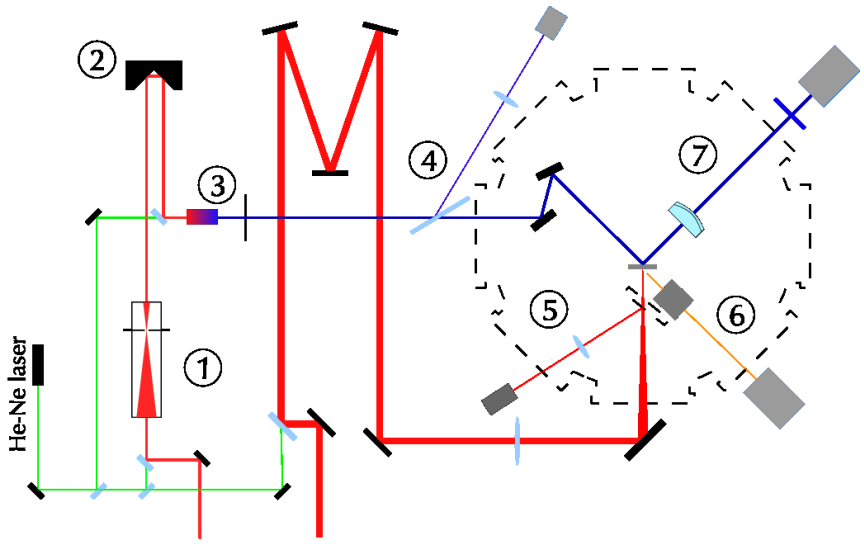

Figure 5.4: Scheme of the experimental setup: 1. telescope and spatial filter, 2. delay line, 3. BBO crystal, 4. glass blade and energy reference camera, 5. focal spot imaging, 6. target focus reference, 7. collection of the diffused light (doublet, filter and camera).

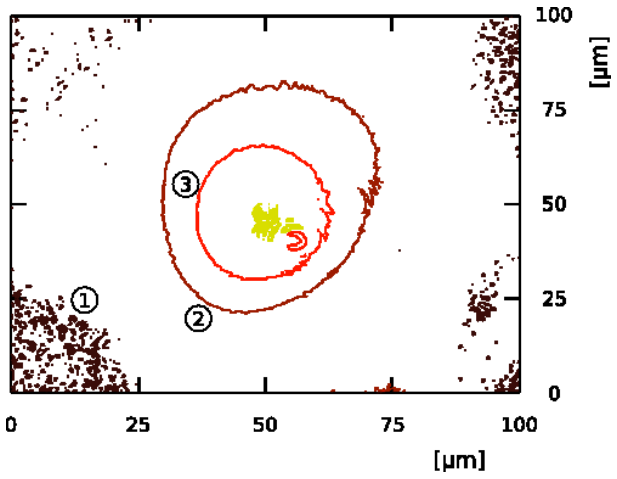

Figure 5.5: Level contours of the focal spot, as measured by the 12bit camera; 1. background, 2. $1/e^2$, 3. FWHM.

of *(i)* increasing the beam intensity without focusing it and *(ii)* enhancing its quality (the transverse profile is cleaned on the focal plane of the first lens by a pinhole of $\phi = 200\mu m$). I decided to avoid the usual procedure in reflectometry measurements of focusing the probe beam on the target surface. In fact, the poor optical quality of

common thin targets, in conjunction with the increased beam divergence, would result in a larger spread of the reflected/diffused light cone.
To be able to analyse the reflectivity map, a precise knowledge of the fluctuations in laser intensity, between the recording of the reference and the shot image, is needed. For this purpose, a glass blade ($150\mu m$, Fig.5.4-4) sends a small part of the *probe* energy to a 12bit camera. For every shot, the integrated image on this camera is used as an intensity reference.
The area on the target surface that corresponds to the pump axis is imaged by an achromatic doublet on a $16bit$ camera (Andor DV434). The doublet is a $f = 150mm$, $\phi = 75mm$; its very large numeric aperture lets us collect the biggest part of the reflected/diffused light and obtain a good magnification. The images in blue light (*probe*) on the camera (Fig.5.4-7) have a final resolution of $2.38\mu m/pix$, producing a total imaged square of $\approx 2.5mm$ by side (1024×1024 pixels).
The alignment of the doublet proved to be very time consuming, and it is done in incoherent white light. A bandpass optical filter (Schott-BG39) is inserted in front of the Andor camera, to minimize the signal that is produced by the plasma self emission and by the infrared light that is diffused in the experimental chamber.
Due to the very high level of inhomogeneities on a typical target surface, getting worse as thickness gets smaller, minor corrections on the Andor camera are necessary. For this purpose the camera is mounted on a micrometric motorized translation and its position corrected when needed. An additional camera (Fig.5.4-6) images the target front surface illuminated in white light with weak magnification ($\approx 2x$) at an angle of 45°. The spot that is produced on this camera by the green alignment beam, collinear with the IR pump beam, is used as an absolute reference on the target position on the focal axis. In fact, given the angle between the focal axis and this imaging axis, a displacement of the target in focus translates into a lateral movement of the imaged spot. This configuration gives a $10\mu m$ sensibility on the target position (i.e. $10\mu m$ of target translation will move the spot on the monitor by a quantity of half of the spot itself). This kind of approach proved to be simple and very effective, in a way that it is used in forthcoming experiments in this manuscript.

Target Alignment The positioning of the target foil along the focus axis is searched for by looking at the surface ionization, that is produced whenever the pump beam interacts, over-threshold, on the thick target holder ($4mm$ aluminum). Moving this

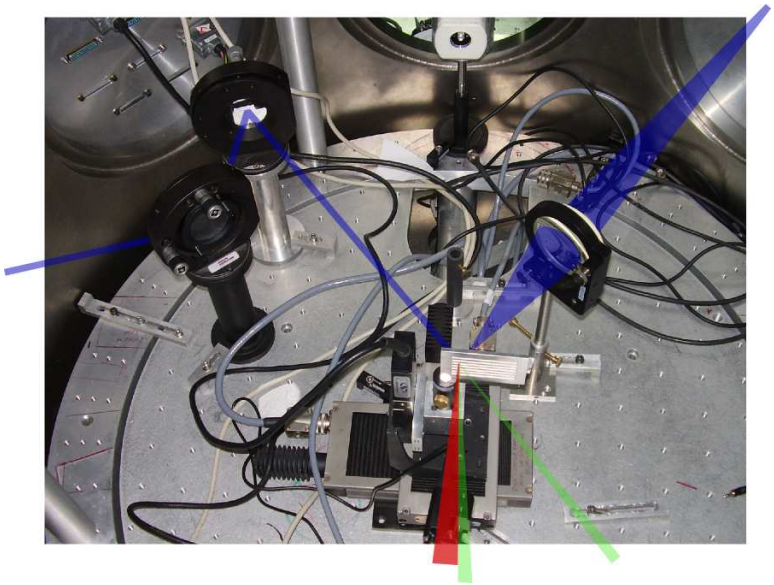

Figure 5.6: Experimental setup with beam paths.

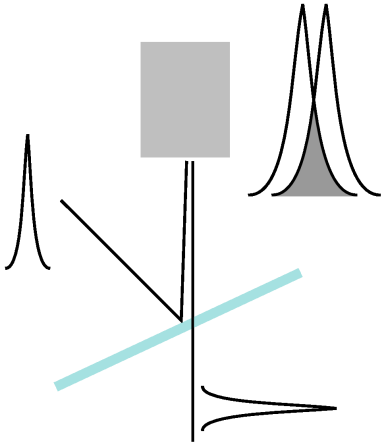

Figure 5.7: Principle of synchronization of the beams.

surface along the pump axis lets us to define a range around the best focus position: its boundaries are defined by the positions where the ionization effect disappears. Neutral densities are added in front of the focusing lens to shrink this range, until smaller than the calculated Rayleigh depth. Its halfway position is taken as a best focus.

Synchronization of the Beams The synchronization condition is searched through the interference condition in the superposition of the two beams. The BBO crystal is removed and a $150\mu m$ thick glass blade in the target holder is used to superpose the two beams on the chip of an 8bit CCD camera. The energy balance between the two is set to enhance the contrast in the interferometry image. The interference condition is found in a range of $1mm$ on the delay line. This means that we're left with an uncertainty on the temporal scale of at least $7ps$. Our supposed $t = 0$ position is set in the middle of this range.

5.4 Experimental Data

The delay time is varied in a range between $0ns$ and $2ns$ and the reflectometry images are recorded without and with pump beam for three different target thicknesses ($3\mu m$, $2\mu m$ and $0.8\mu m$). A third image is taken after the pump shot; an example of a set of experimental images is presented in Fig.5.8.

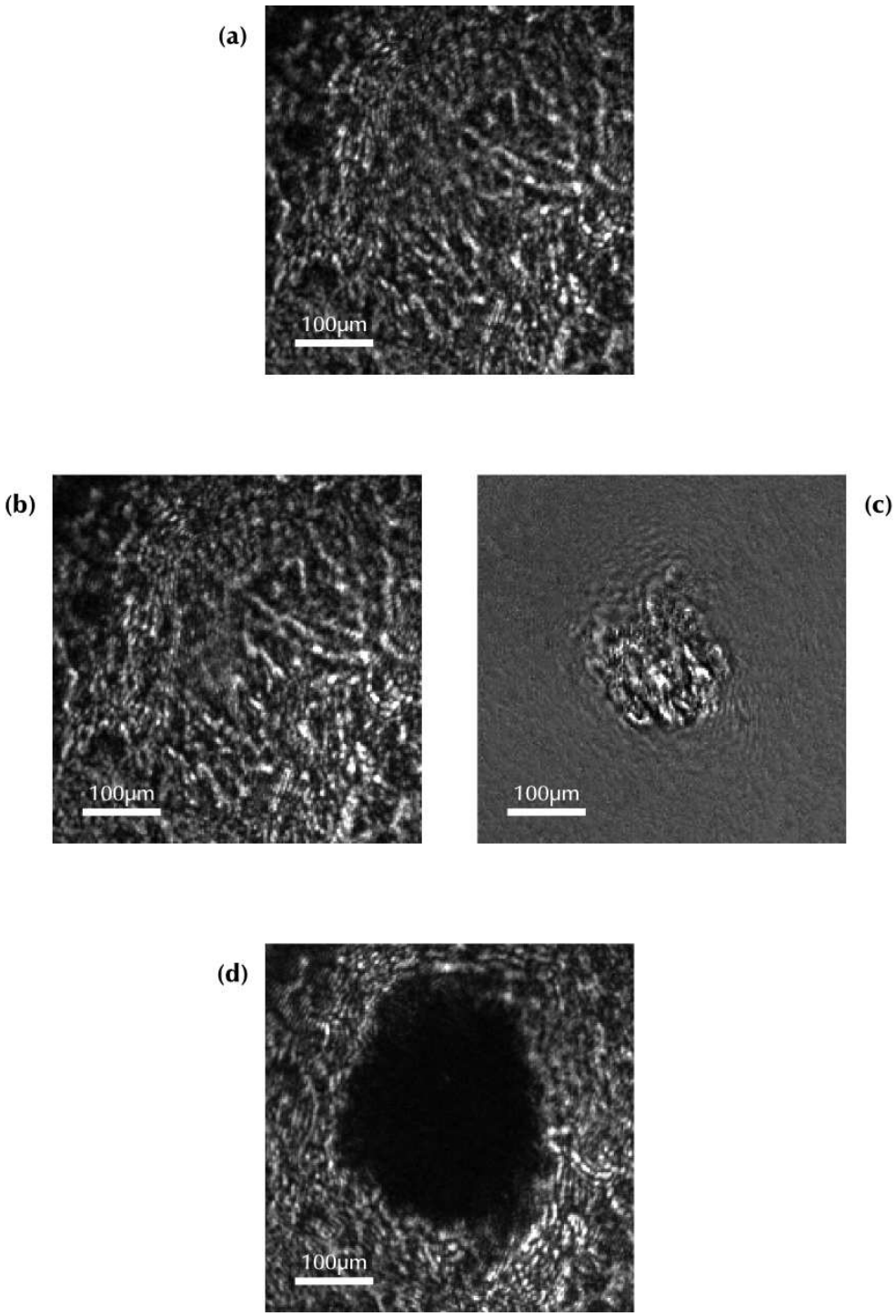

Figure 5.8: Cuts from a set of reflectometry images of a $3\mu m$ target after a delay of $90mm$ ($600ps$) from the *pump* pulse. (a) Reference image. (b) Reflectometry during the *pump* shot; no apparent deformation is visible. (c) Pixel to pixel ratio between (b) and (a): except from the shot area, an almost flat surface at $R \approx 1$. (d) Image of the back surface long time after the shot. 68

The surface of the target has no optical quality, which results in the formation of a homodyne speckle field (Fig.5.8-a,b,d) that is produced by the interference of the – coherent – light source on the structures of the surface that have a size comparable to the wavelength. When the *pump* laser is shot, no clearly visible perturbation is present on a ns timescale, other than a deformation (Fig.5.8-b) in the speckle field, which depends on the delay time. If the pixel-wise ratio

$$\tilde{R} = \frac{I_{shot}(x,y)}{I_{ref}(x,y)} \tag{5.9}$$

between the shot and the reference image is calculated, some deformation structures start to appear, surrounded by the almost[4] constant plane $\tilde{R} = 1$; on purely qualitative basis, we can divide the obtained $\tilde{R}$ maps in three types (Fig.5.9) as delay time increases:

1. **no perturbation:** there is no observable perturbation in the $\tilde{R} = 1$ surface;
2. **speckles deviation:** the shot area shows peaks of relative reflectivity both lower and higher than 1 but integrals show no net energy absorption. The peaks might be originated by the rigid translation of speckles around the shock breakout area;
3. **absorption:** inside the speckles perturbation area appears a clean, almost circular, darker structure.

The boundary between different types of images is found to be dependent on the target thickness: their scaling is depicted in (Fig.5.10).

[4]This neglects intensity fluctuations on the image that are produced by laser instability and that show a low spatial frequency.

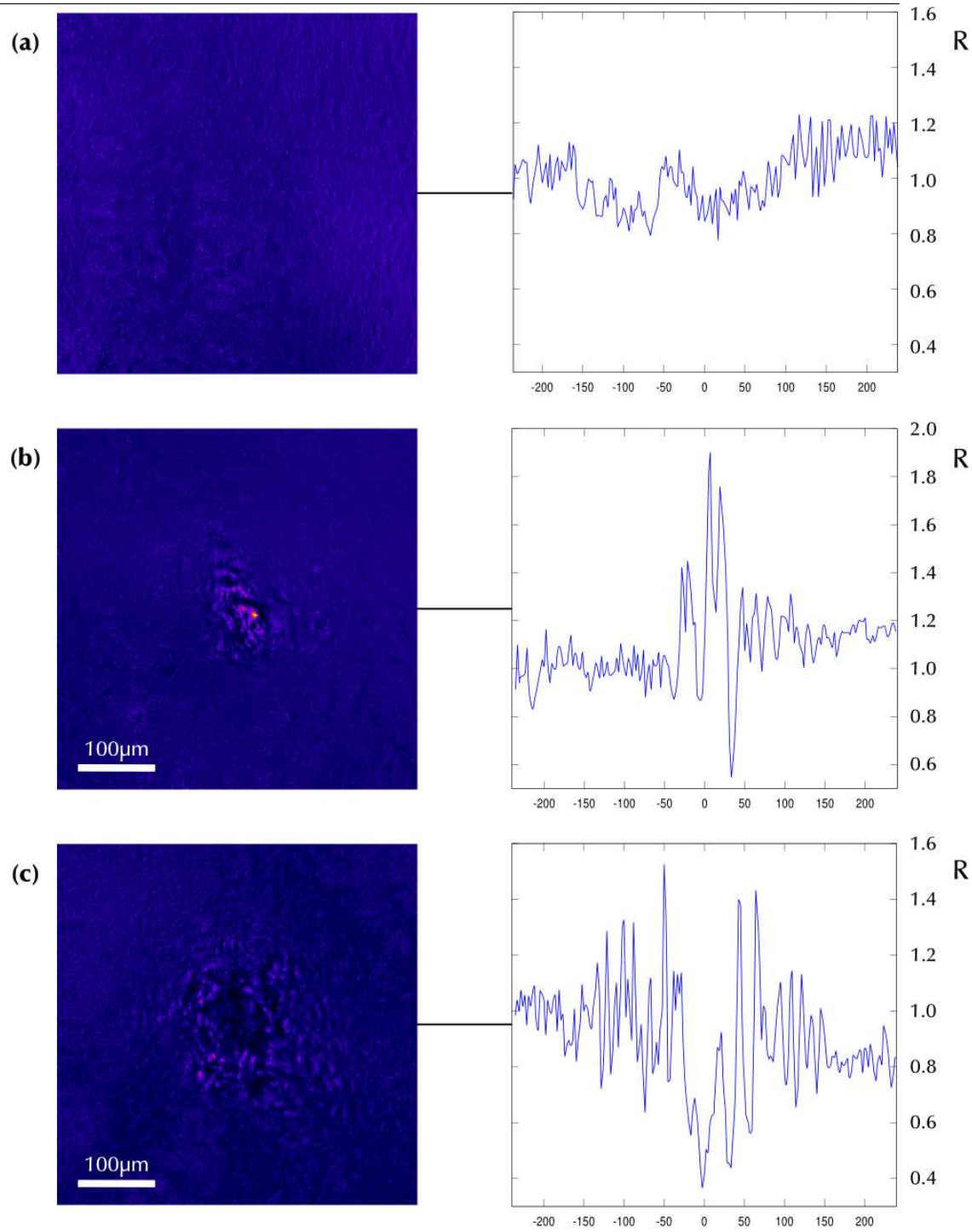

Figure 5.9: $\tilde{R}$ maps (left) and horizontal cuts (right) for three different delays on a $2\mu m$ target; (a) $t = 150ps$ no perturbation is present; (b) $t = 350ps$ speckles deformation results in lighter ($\tilde{R} >> 1$) and darker ($\tilde{R} < 1$) areas, without any net energy absorption; (c) darker areas are clearly visible and a net energy absorption is measurable.

A different behaviour is observed on the $800nm$ target. Here the perturbation appears

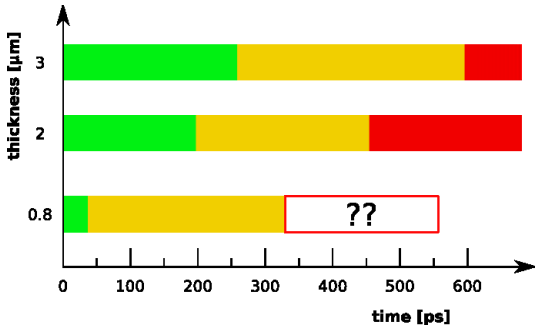

Figure 5.10: Time boundaries between different types of rear surface perturbation for different target thicknesses. Green, Yellow and Red bands represent respectively maps like Fig.5.9-a/b/c. For the $800nm$ case, no clear transition to "red" type was observed in the searched timescale.

within the first $100ps$ as a "deformation-like" image and no transition to the "absorption-like" is observed in the searched timescale. Instead, the perturbed area expands radially without a precisely defined structure.

5.5 Analysis of the Experimental Data

The images are treated numerically. At first the parameters of each shot are measured from the $\tilde{R}$ image; the $shot/reference$ map is filtered in its $2D$ Fourier plane [5]. The purpose of this filter is to eliminate every feature belonging to the target spatial characteristics, its transverse fluctuations and camera electronic noise. The interest of this filtering, while not conserving the experimental information of reflectivity, is to precisely determinate, in a self consistent way for the entire dataset, the geometrical parameters of the shocked area: the position of its center, the diameter of the perturbation (Fig.5.8-*upper*) and the laser reference area. The laser reference area is a square aside of the shocked region where no influence from the *pump* laser is supposed to have happened; its integral in energy, from the untreated images, is used to normalize the total contained energy between the different shots, getting rid of laser fluctuations.
The reflectivity is finally calculated from the ratio between the total energy contained in the shocked region from the two, reference and shot, images; the ratio is renormalized to the ratio of integrals from the two check areas:

[5] I used a 100 pixels FWHM, 10^{th} order bi-dimensional super-gaussian filter.

$$R_{exp} = R_{cold\,Al} \cdot \frac{E_{hole,shot}}{E_{hole,ref}} \cdot \frac{E_{check,ref}}{E_{check,shot}} \tag{5.10}$$

The integration is done via standard trapezoids method. Note that this calculation gives only the difference in reflectivity between the perturbed and the unperturbed case; in order to plot it on an absolute scale, it has to be renormalized to the reflectivity of cold aluminum, $R_{cold\,Al} = 0.98$.

In Fig.5.11 is shown the evolution of the size of the perturbation on the surface versus

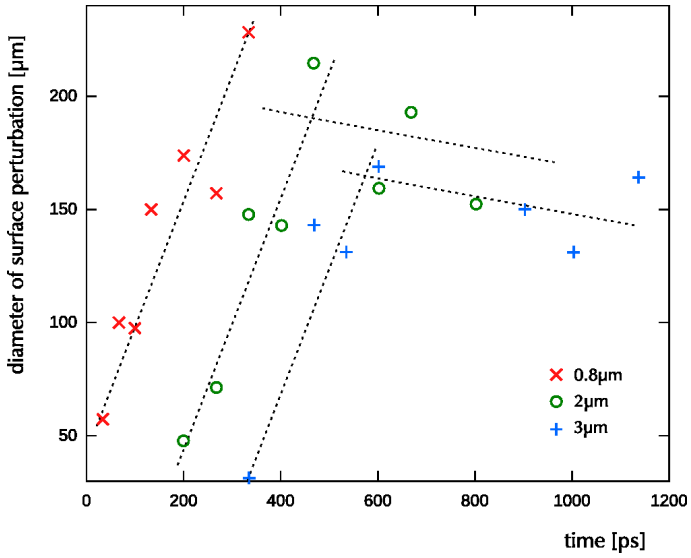

Figure 5.11: Diameter of the perturbation on the rear face of the target measured on the $\tilde{R}(x, y)$ images.

time. The boundaries are measured on the filtered $\tilde{R}$ image (defined by (5.9)). There is a qualitative difference between the target thicknesses. In fact both the thicker targets show a "hole" that grows in diameter until a quasi-static value is reached. The $800nm$ target, on the contrary, doesn't settle, and produces a continuously growing structure until its size reaches the final hole diameter (like the one shown in Fig.5.8-d). No precise absorbing structure (like Fig.5.9-c) is ever produced. For this reason no further data acquisition and analysis is performed on the $800nm$ data after $t = 350ps$ (see 5.6).
For the other two thicknesses the reflectometry results are summarized in Fig.5.12 and Fig.5.13.

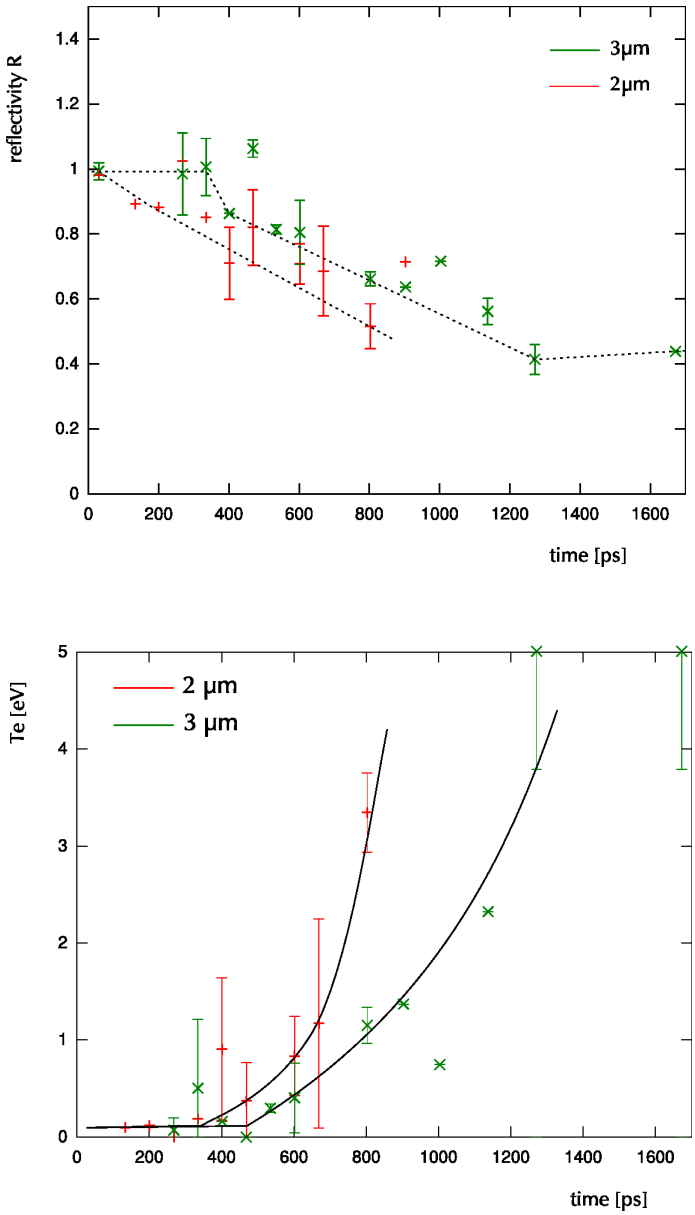

Figure 5.12: *(upper)* The experimental value of R as defined in (5.2) and calculated according to (5.10), for the two thicker targets. *(lower)* Evolution of the electron temperature T_e from the experimental points in the upper plot. The highest point for the $3\mu m$ target are limited in electron temperature by the minimum reflectivity that bulk aluminum in the considered conditions can have ($R = 0.51$ at $T_e = T_i = 5.2eV$).

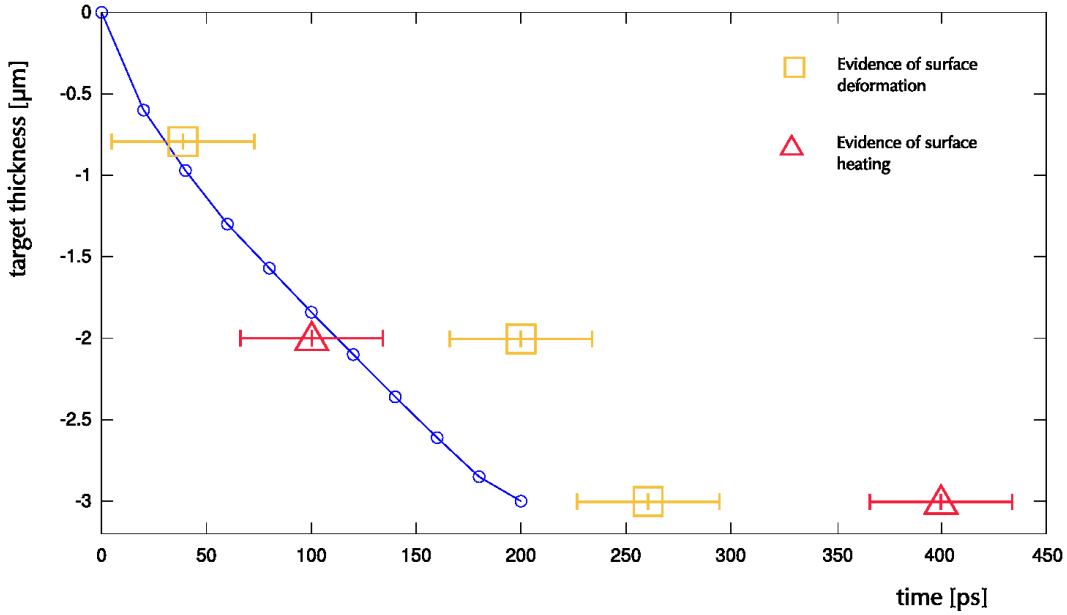

Figure 5.13: Synthesis of the propagation of the shock wave through the metal target. The blue circles represent the propagation of the shock wave in an infinite bulk (extrapolation from the hydrodynamic simulations in 4.4). The yellow points represent the moment where a variation becomes first visible on the $\tilde{R}$ maps. The red points fix the moment when the reflectivity starts falling from the analysis in Fig.5.12-*upper*.

5.6 Discussion

The experimental measurements show an evolution in time which is consistent with the timescale that is obtained from simulations.

The experimental points in Fig.5.13 show a qualitative difference between the three thicknesses. The yellow squares represent the position of the delay line when a structure becomes visible in the $\tilde{R}$ maps, meaning a deformation in the speckle field. The red triangles mark the point where the experimental plots in Fig.5.12 show a fall in reflectivity from the unperturbed value.

The $3\mu m$ targets experience a deformation before a measurable absorption happens. The $2\mu m$ targets show light absorption before a visible deformation of the surface. The moment the absorption starts is consistent with the arrival of the shock wave. The difference between the two behaviours might be due to the different importance of the ion heating. On the $3\mu m$ target the ion heating may happen later than the $2\mu m$, which could explain why on the thicker one, the decrease in reflectivity happens later.

Finally the $800nm$ target: on the point of view of the scale of time, the surface starts to be perturbed in accord with the hydrodynamic simulation. The evolution that follows (the formation of an undefined, expanding structure) can be explained by a consideration. Targets thinner than $1.5\mu m$ are not guaranteed (by the manufacturer) to be light-tight, which means that the production process cannot achieve a real metallic foil, but more probably a cluster of smaller structures. When the structure is stressed it might behave in a different way than a real metallic foil[6].

As for the timescale of the perturbation, the target thickness is traversed by the shock wave at a speed of $3\mu m$ in $200ps$ which motivates, for the forthcoming experiments of proton acceleration, the boundary of

$$d[\mu m] > 15 \cdot \Delta t[ns] \tag{5.11}$$

where d is the thickness of the target and Δt is the distance, in ns, from the beginning of the over-threshold part of the pedestal and the main femtosecond peak. Moreover the information here contained enables us to correlate the gradient scale length that is produced on the illuminated surface and the position of the shock in the bulk (see Fig.4.16 along with Fig.5.13).
As for the characterization of the target surface in presence of the breakout of a shock, the simple reflectometry doesn't allow to obtain sufficient informations. In fact, once the shock has broken out, a second expansion begins. In presence of a density gradient, the simple, single beam, reflectometry measurement cannot distinguish between absorption due to the electron temperature and absorption in the plasma gradient. During our experiment we believe the delay time to be short enough to neglect the formation of a density gradient.
With the aim of studying the effect of laser pedestal in proton acceleration experiments, a precise characterization of the gradients and temperatures should be undertaken. For example, a complete analysis of homodyne speckle fields, like those registered in images (like Fig.5.8), could give a precise mapping of the surface deformation[7] which is reported [57] to be correlated with the angle of emission of the accelerated ions.

[6]This fact seems to be specially true for GoodFellow foils at $800nm$, which shows unpredictable behaviour in the proton acceleration experiment too.

[7]This could be done, for example, by a wavelet analysis on the homodyne speckle field with proper test functions.

Finally, the experimental campaign underlines the importance of a deeper study of the structure of thinner targets and in which ways it could affect the ion acceleration mechanisms.